Water Budget of Typhoon Nari (2001)

MING-JEN YANG

*Department of Atmospheric Sciences, and Institute of Hydrological and Oceanic Sciences, National Central University,
and Taiwan Typhoon Flood Research Institute, Chung-Li, Taiwan*

SCOTT A. BRAUN

NASA Goddard Space Flight Center, Greenbelt, Maryland

DENG-SHUN CHEN

Department of Atmospheric Sciences, National Central University, Chung-Li, Taiwan

ABSTRACT

Although there have been many observational and modeling studies of tropical cyclones (TCs), the understanding of TCs' budgets of vapor and condensate and the changes of budgets after TCs' landfall is still quite limited. In this study, high-resolution (2-km horizontal grid size and 2-min data interval) model output from a cloud-resolving simulation of Typhoon Nari (2001) is used to examine the vapor and condensate budgets and the respective changes of the budgets after Nari's landfall on Taiwan. All budget terms are directly derived from the model except for a small residual term. For the vapor budget, while Nari is over the ocean, evaporation from the ocean surface is 11% of the inward horizontal vapor transport within 150 km of the storm center, and the net horizontal vapor convergence into the storm is 88% of the net condensation. The ocean source of water vapor in the inner core is a small portion (5.5%) of horizontal vapor import, consistent with previous studies. After landfall, Taiwan's steep terrain enhances Nari's secondary circulation significantly and produces stronger horizontal vapor import at low levels, resulting in a 22% increase in storm-total condensation. Precipitation efficiency, defined from either the large-scale or microphysics perspective, is increased 10%–20% over the outer-rainband region after landfall, in agreement with the enhanced surface rainfall over the complex terrain.

1. Introduction

Malkus and Riehl (1960) indicated that the ratio of the moisture source from the ocean to the net horizontal import of moisture into a tropical cyclone (TC) was less than 10%. Despite the small percentage, the ocean moisture source plays an important role in the generation and maintenance of TCs (Riehl and Malkus 1961; Kurihara 1975; Hawkins and Imbembo 1976; Zhang et al. 2002).

Kurihara (1975) examined the water vapor budget of a simulated axisymmetric TC and found that the dominant budget terms were the total (horizontal plus vertical) advection and condensation. Calculating the volume-integrated budget within a 500-km radius, Kurihara indicated that the evaporation from the ocean surface was 20% of the condensation and 25% of total advection, respectively. For the inner core region, ocean evaporation was very small compared to either condensation or advection. For the outer region, on the other hand, evaporation from the ocean surface supplied substantial moisture and latent heat fluxes to the atmosphere, ultimately resulting in a large horizontal transport of moisture into the inner core.

Zhang et al. (2002) calculated thermodynamic budgets from a 6-km grid simulation of Hurricane Andrew (1992) and expressed the budgets in advective form. They indicated that horizontal advection tended to transport drier air from the outer region into the core in the marine boundary air, and transport moist air from the eye to the eyewall within the low-level outflow above the boundary layer. Within the eyewall, the moisture transport by

Corresponding author address: Dr. Ming-Jen Yang, Department of Atmospheric Sciences, National Central University, 300 Chung-Da Road, Chung-Li, 320, Taiwan.
E-mail: mingjen@cc.ncu.edu.tw

vertical advection was larger than that by horizontal advection.

There are many studies of water vapor budgets of TCs; on the other hand, only a few studies have been conducted for the condensed water budgets of TCs. Using radar data, Marks (1985) estimated that 60% of the inner-core ($r < 110$ km) rainfall of Hurricane Allen (1980) was classified as stratiform rainfall and that the water vapor convergence into the eyewall was more than twice the volumetric rainfall. Marks and Houze (1987) divided the radar echo area of Hurricane Alicia (1983) into two regions (the eyewall and the outer stratiform precipitation area), and found that 62% of the rain within the radar volume ($r < 40$ km) fell in the stratiform region ($r > 20$ km). They further estimated that the condensation in the stratiform region was 3 times the water mass transport outward from the eyewall, indicating the dominance of the in situ production of water.

Gamache et al. (1993) conducted a detailed water budget study using dual-Doppler radar and aircraft data collected for Hurricane Nobert (1984). Based on a large value of the estimated vapor diffusion across the bottom boundary (~ 500 m) of the analysis volume, they estimated that approximately 40% of the vapor converging into the budget volume ($r < 37.5$ km) had evaporated from the ocean surface, an amount significantly larger than that found in previous studies.

Braun (2006) computed the water budget from a 2-km grid simulation of Hurricane Bonnie (1998). He indicated that a large fraction of the condensation in the eyewall occurred in convective hot towers while condensation in the outer region occurred more often in weaker updrafts in stratiform precipitation areas. For the mature stage of Bonnie, cloud condensate was consumed as rapidly as it was produced. Cloud droplets were maximized at the top of the boundary layer and within the melting layer, where cooling from melting enhanced condensation. Snow particles ejected outward from the eyewall seeded the outer regions and increased stratiform precipitation development locally through the microphysical processes of vapor deposition and aggregation.

Typhoon Nari struck Taiwan on 16 September 2001, bringing heavy rainfall (with 3-day-total rainfall of more than 1400 mm), strong wind gusts, and flash floods. It caused severe economic and societal impacts, including the loss of 92 human lives (Sui et al. 2002). Because of the tremendous rainfall and the severe disaster produced by Nari, several studies have focused on Nari by utilizing observations and modeling. For example, the precipitation efficiency of Typhoon Nari over the ocean was discussed in Sui et al. (2005), and the flooding caused by Nari was examined in Li et al. (2005). Yang et al. (2008, hereafter YZH) conducted a quadruply nested–grid fifth-generation

Pennsylvania State University–National Center for Atmospheric Research Mesoscale Model (MM5) simulation for Nari with the finest grid size of 2 km and showed that the model reproduced reasonably well the kinematic and precipitation features. These include the storm track, the size and contraction of the eye and eyewall, the spiral rainbands, the rapid pressure rise (~ 1.67 hPa h^{-1}) during landfall, and the nearly constant intensity after landfall. In addition, the model captured the rainfall distribution and some local maxima associated with Taiwan's orography. Yang et al. (2011) further examined the structure changes and terrain-induced storm asymmetries after Nari's landfall on Taiwan by comparing the full-terrain control run with the reduced-terrain sensitivity simulations.

To better understand the evolution of clouds and precipitation in Typhoon Nari during its landfall on Taiwan, budgets for vapor, cloud, and precipitation are conducted in this study by analyzing the MM5 output from YZH with high spatial and temporal resolutions (2-km horizontal grid size and 2-min output interval). The first objective of this study is to investigate the evolution of the water vapor, cloud, and precipitation budgets during Nari's landfall on Taiwan, especially for the transition from the more axisymmetric structure over the ocean to the highly asymmetric structure over the mountains. The second objective is to understand what portions of the heavy rainfall from Nari were produced in situ, that is, locally generated by condensation and melting, and what portions of rainfall were produced by moisture transported from the surrounding oceanic environment. The third purpose is to examine whether the precipitation efficiency is indeed increased after Nari's landfall on the mountainous island of Taiwan. Through the analyses of water vapor, cloud, and precipitation budgets, we gain physical insights into how vapor, clouds, and precipitation were generated within Nari and how microphysical processes were modified as Nari encountered the mountainous topography of Taiwan. Under the constraints of model deficiencies and physics uncertainties, the physical insights and understanding gained from this water budget study based on model diagnostics may help improve the microphysical parameterization of TCs in the future.

2. Model simulation

a. Model description

In this study, we analyze the control simulation results from the finest 2-km grid of the simulation described in YZH. The 2-km grid simulation, having $271 \times 301 \times 32$ grid points on the (x, y, σ) grid and covering a horizontal
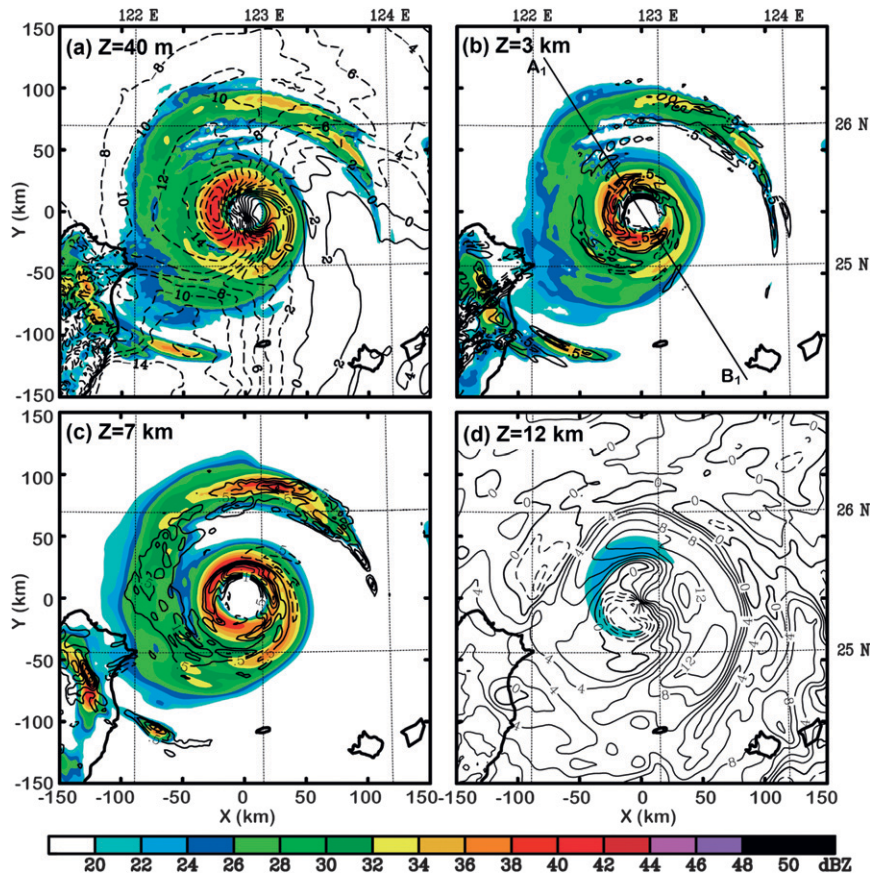
FIG. 1. Color shading indicates time-averaged (13–14 h) simulated radar reflectivity at (a) 40 m, (b) 3 km, (c) 7 km, and (d) 12 km on the 2-km grid. Contour overlays in (a) and (d) are storm-relative radial velocities drawn at 2 m s^{-1} intervals. Contours in (b) and (c) are vertical velocities drawn at 0.5 m s^{-1} intervals with the 0 contour omitted. Solid (dashed) lines indicate positive (negative) values. The straight line A$_1$B$_1$ in (b) indicates the horizontal position of the vertical cross sections in Fig. 2.

area of 540 km × 600 km, was performed by using the initial and lateral boundary conditions provided by the output of the 6-km grid, which was obtained by running the triply nested domains separately (54, 18, and 6 km). The 2-km grid simulation uses the 3-ice microphysics scheme of Reisner et al. (1998), which solves for the mixing ratios of water vapor q_v, cloud water q_l, cloud ice q_i, rainwater q_r, snow q_s, and graupel q_g. (See YZH for a detailed description of the model design and setup.)

Two stages of Nari's development are chosen for the present study: an ocean stage during 13–14 h of the simulation (0100–0200 UTC 19 September 2001, with few influences from land) and a landfall stage during 23.5–24.5 h (1130–1230 UTC 19 September 2001, with half of Nari's circulation over Taiwan). These times are 8 h prior to and 1.5 h after landfall, respectively. Most fields are averaged hourly from output at 2-min intervals to show

more persistent mesoscale structures by reducing small-scale temporal fluctuations.

b. Simulated structures

Color shading in Fig. 1 indicates the time-averaged (13–14 h) simulated radar reflectivity at 40 m, 3 km, 7 km, and 12 km, respectively, during the oceanic stage. Intense precipitation occurs within the eyewall, and a principal rainband is located to the west and north of the eyewall. Strong radial inflow with a peak intensity of −26 m s^{-1} is near the surface (Fig. 1a) and radial outflow with a peak value of 14 m s^{-1} is found at the upper levels (Fig. 1d). Strong convective updrafts occur inside the inner core, and relatively weaker but wider mesoscale updrafts are in the principal rainband (Figs. 1b,c).

Figure 2a shows the vertical structure of time-averaged (13–14 h) simulated radar reflectivity across Nari along
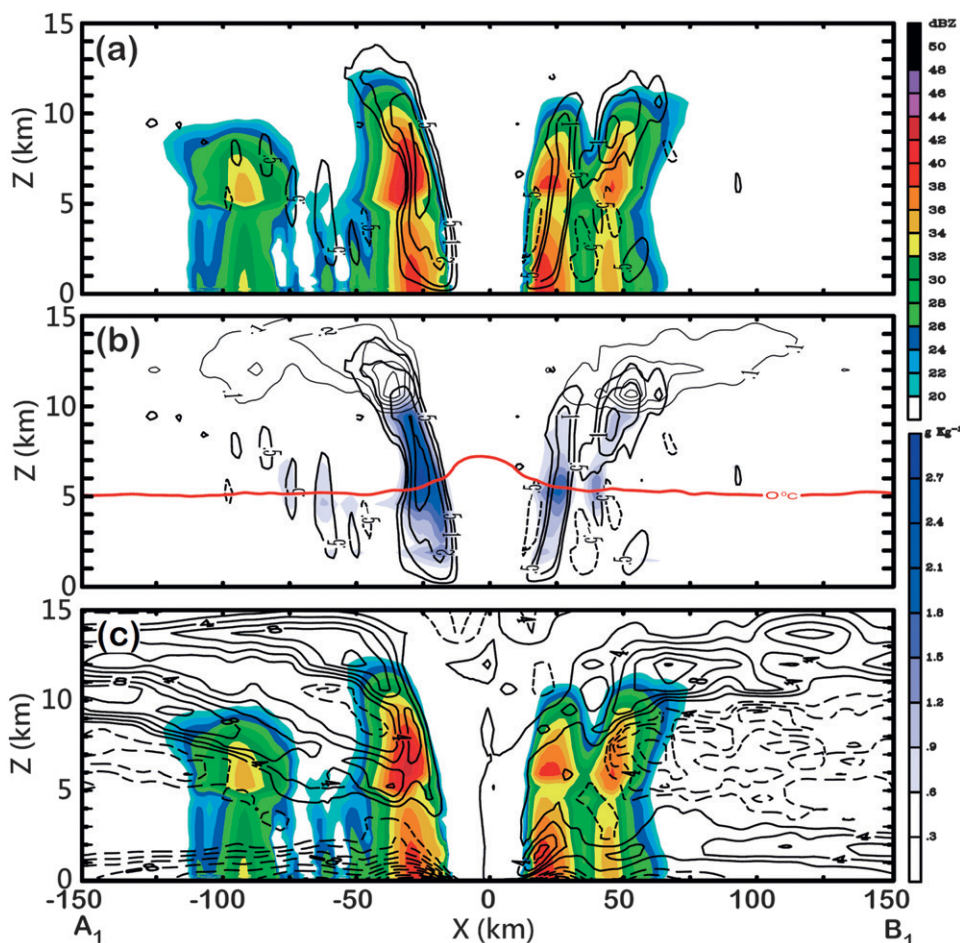
FIG. 2. (a),(c) Color indicates the time-averaged (13–14 h) simulated radar reflectivity and (b) blue shading indicates cloud water mixing ratio along the A_1B_1 cross section (see Fig. 1 for the horizontal position). Thick contours in (a) and (b) are vertical velocity drawn at 1 m s^{-1} intervals with the 0 contour omitted and extra contours at ±0.5 m s^{-1}. Thin contours in (b) are cloud ice mixing ratio drawn at 0.1 g kg^{-1} intervals. Red line in (b) is the 0°C isotherm. Contours in (c) are storm-relative radial velocity at 2 m s^{-1} intervals. Solid (dashed) lines indicate positive (negative) values.

the A_1B_1 (cross track) cross section, which clearly displays the outward-tilted eyewall and rainbands farther outward from the center. Deep updrafts with a peak intensity of 3.5 m s^{-1} occur in the eyewall; weaker updrafts (downdrafts) are at upper (lower) levels in the outer rainbands (Fig. 2b). At lower levels, the radial inflow in the northwestern quadrant (left half of Fig. 2c) is deeper and stronger than that in the southeastern quadrant (right half of Fig. 2c). Radial outflow with peak values of 10–12 m s^{-1} occurs at upper levels while strong midlevel outflow can be seen in the northwestern quadrant (left half of Fig. 2c). Abundant supercooled liquid water (with $q_l > 2$ g kg^{-1}) associated with deep updrafts is found inside the eyewall (Fig. 2b).

Because Typhoon Nari maintained a quasi-axisymmetric structure while it was over the ocean, it is more meaningful

to look at the azimuthally *averaged* structures of Nari in terms of its kinematics, cloud, and precipitation fields (Fig. 3). The average tangential wind is maximized at $r = 20$ km, with a peak intensity of slightly greater than 55 m s^{-1} at the top of boundary layer (Fig. 3a). Radial velocities are primarily inward at lower levels and outward at upper levels, with most of the inflow concentrated in the boundary layer (Fig. 3b). Updrafts reach an altitude of 13 km within the vertically tilted eyewall, and downdrafts occur at the interface between the eye and eyewall (Fig. 3c). Inside the eyewall, the atmosphere is moistened by the upward transport of moisture from deep updrafts, and a similar amount of moistening is also found below 5 km inside the eye; on the other hand, strong drying by mesoscale downdrafts is found in the outer-rainband region with $r > 60$ km (Fig. 3d). Cloud water is maximized

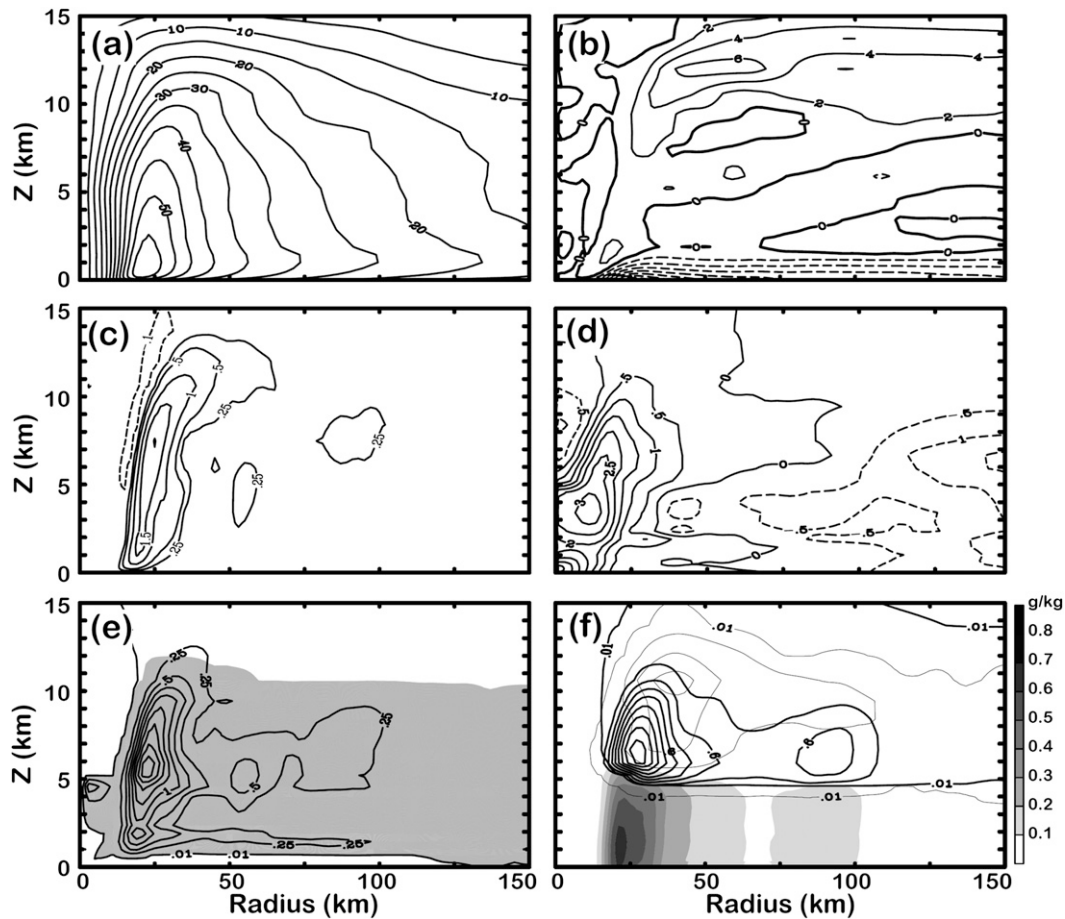FIG. 3. Azimuthally and temporally (13–14 h) averaged fields for (a) tangential velocity, 5 m s^{-1} intervals; (b) radial velocity, 2 m s^{-1} intervals; (c) vertical velocity, 0.5 m s^{-1} intervals with the 0 contour omitted and 0.25 and -0.1 m s^{-1} contours added; (d) water vapor mixing ratio departure from the domain-averaged value, 0.5 g kg^{-1} intervals; (e) cloud water and ice mixing ratios, 0.25 g kg^{-1} intervals with an extra contour at 0.01 g kg^{-1} and shading indicating cloud liquid water $>$0.01 g kg^{-1}; and (f) rain (shading), snow (thin contours), and graupel (thick contours) mixing ratios, 0.3 g kg^{-1} intervals with an extra contour at 0.01 g kg^{-1}.

within the eyewall, near the top of boundary layer, and near the melting layer at $z = 5$ km; cloud ice is maximized at the altitude of 12 km (Fig. 3e). The rainwater maximum is below and slightly inward of the graupel maximum in the eyewall, indicating a large production of raindrops by the melting of graupel particles. Another pair of rainwater and graupel maxima is in the outer rainbands. Snow peaks near a 10-km altitude in the eyewall, approximately 3–4 km higher than graupel (Fig. 3f).

After landfall, Taiwan's steep terrain imposes a large degree of asymmetry on Nari's kinematic and precipitation structures (Fig. 4). A terrain-sensitivity experiment indicates that the asymmetry is greatly reduced if Taiwan's terrain is totally removed (see Figs. 10 and 11 of Yang et al. 2011). Low-level radial inflow is stronger than that seen over the ocean, especially near the coast, because of the enhanced flow convergence and storm retardation caused

by increased friction (Fig. 4a; note that the contour interval is 4 m s^{-1} in Fig. 4a but 2 m s^{-1} in Fig. 1a). Vertical updrafts and downdrafts are also enhanced over the island, with more cellular structures associated with flow over the small ridges and valleys within the Central Mountain Range (CMR; see Figs. 4b,c). Greater upper-level radial outflow and inflow variations are found during landfall (Fig. 4d).

Because of the strong asymmetry of Nari's structure after landfall, it is less representative to show the symmetric fields at this time. Instead, we will illustrate Nari's asymmetric structures from the time-averaged (23.5–24.5 h) simulation results in two vertical cross sections, that is, A_2B_2 (along track) and C_2D_2 (cross track) cross sections, respectively.

In the A_2B_2 cross section, which cuts through the major peak (Mount Snow) in the northern CMR, the tangential
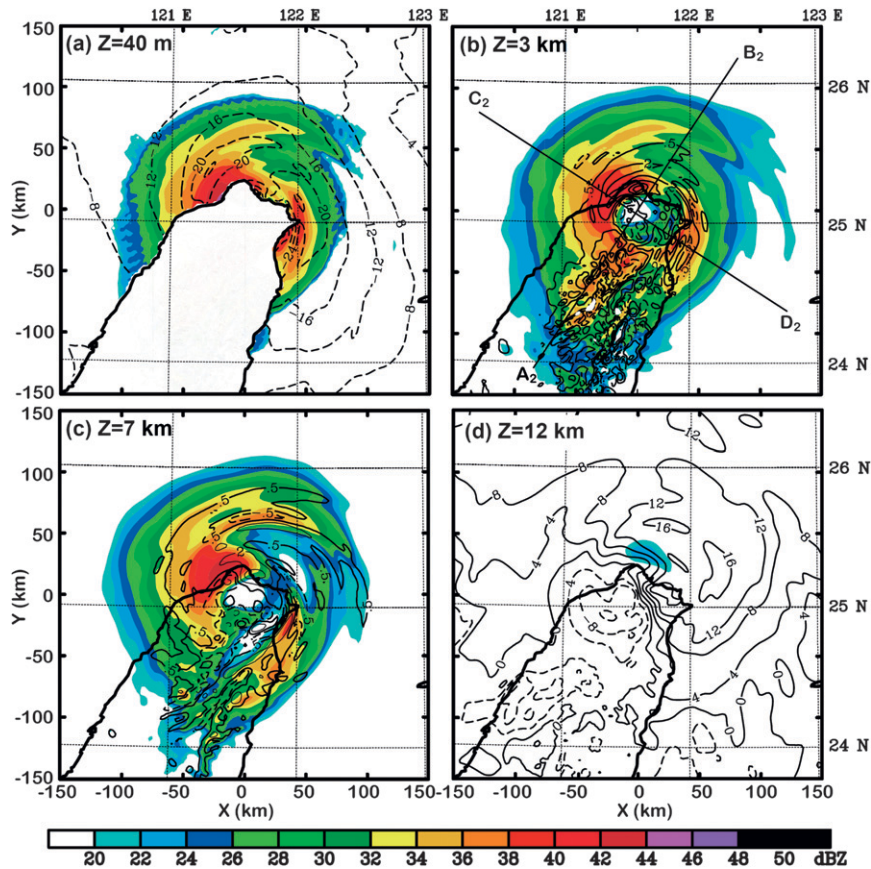
FIG. 4. Color shading indicates time-averaged (23.5–24.5 h) simulated radar reflectivity at (a) 40 m, (b) 3 km, (c) 7 km, and (d) 12 km on the 2-km grid. Contour overlays in (a) and (d) are storm-relative radial velocities drawn at 4 m s^{-1} intervals. Contours in (b) and (c) are vertical velocities drawn at 2 m s^{-1} intervals with the 0 contour omitted and extra contours of -0.5 and 0.5 m s^{-1} added. Solid (dashed) lines indicate positive (negative) values. The straight lines A_2B_2 and C_2D_2 in (b) indicate the horizontal position of the vertical cross sections in Figs. 5 and 6, respectively.

wind is stronger near the coast (peaking near 60 m s^{-1}) than over land ($\sim$55 m s^{-1}) (Fig. 5a) as a result of stronger convergence of absolute angular momentum near the coast and enhanced friction by terrain over land. Intense radial inflow occurs at lower levels and outflow at upper levels near the coast and over the ocean. Sloping radial outflow occurs at midlevels above the northern CMR, transporting hydrometeors outward to broaden the surface precipitation area (Fig. 5b). Updrafts are stronger (peaked at 5 m s^{-1}) and more upright near the coast, but weaker (peaked at 2–4 m s^{-1}) and outward tilted over the terrain. Several peaks of updrafts and downdrafts are found above the mountain, which are produced by the strong rotational winds impinging on the steep CMR (Fig. 5c). Copious moisture (with $q_v > 16$ g kg^{-1}) is pushed upward to 2-km altitude by the flow over the terrain (Fig. 5d). Abundant cloud water droplets (gray shading) are over the CMR, while over the coast and ocean, cloud

water droplets are at much higher altitudes. Cloud ice is located primarily above a 10-km altitude, with more ice particles above the deep updrafts near the coast (Fig. 5e). More rain occurs above the northern CMR compared to over the coast and ocean (Fig. 5f). Similarly, abundant graupel particles are found at altitudes of 5–8 km over the steep terrain and above rainwater maxima.

In the C_2D_2 cross section, which cuts through the small hill over Keelung, some noticeable structural differences from the A_2B_2 cross section are found. Tangential winds are stronger (peaking near 57 m s^{-1}) near the coast than those ($\sim$49 m s^{-1}) above the small hill (Fig. 6a), likely because the air over the hill is coming off of the island and has experienced significant friction. In addition to the low-level radial inflow and upper-level outflow, intense radial outflow is also found at midlevels, suggesting more shallow updrafts and midlevel detrainment (Fig. 6b). Deep updrafts and downdrafts are found in the eyewall and
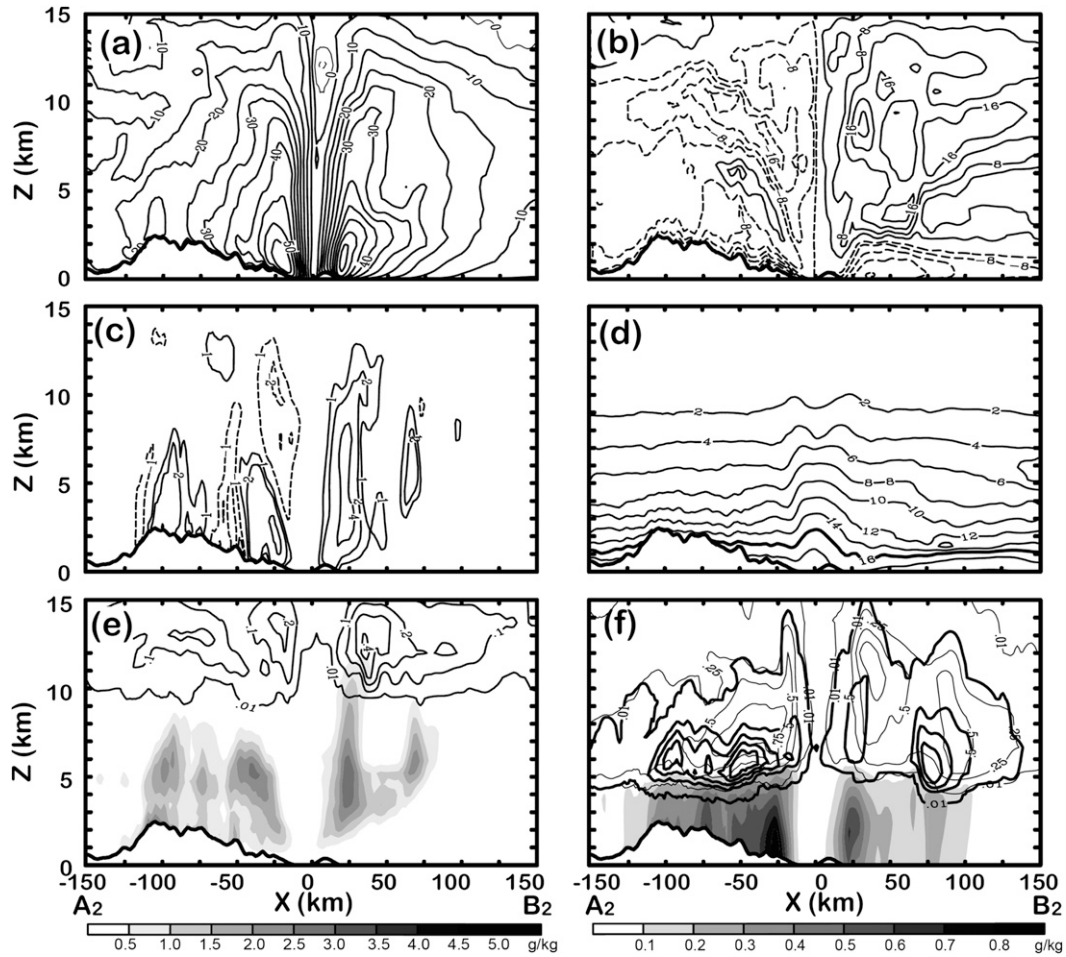
FIG. 5. Vertical cross section (A_2B_2) of temporally (23.5–24.5 h) averaged fields for (a) tangential velocity, 5 m s^{-1} intervals; (b) radial velocity, 4 m s^{-1} intervals with the 0 contour omitted; (c) vertical velocity, 2 m s^{-1} intervals with the 0 contour omitted and −1 and 1 m s^{-1} contours added; (d) water vapor mixing ratio, 2 g kg^{-1} intervals with a thick contour for 16 g kg^{-1}; (e) cloud water and ice mixing ratios, 0.1 g kg^{-1} intervals with an extra contour at 0.01 g kg^{-1} for cloud ice and shading for cloud liquid water; and (f) rain (shading), snow (thin contours), and graupel (thick contours) mixing ratios, 0.25 g kg^{-1} intervals with an extra contour at 0.01 g kg^{-1} for snow mixing ratio, 0.5 g kg^{-1} intervals with an extra contour at 0.01 g kg^{-1} for graupel mixing ratio.

above the small hill (Fig. 6c). Highly moist air (with $q_v >$ 19 g kg^{-1}) is located inside the eye (Fig. 6d). Cloud water mixing ratios peak at midlevels within the eyewall, with ice abundant at upper levels (Fig. 6e). Large rain mixing ratios occur in the northwestern quadrant (left half of Fig. 6f), compared to the southeastern quadrant (right half of Fig. 6f). Similarly, greater graupel mixing ratios are found in the northwestern quadrant than the southeastern quadrant.

3. Budget formulation

All water budget calculations are based on the governing equations used in MM5 (Dudhia 1993; Grell et al. 1995). Following Liu et al. (1999), Zhang et al. (2000, 2001), and Braun (2006), we will discuss the water budget

of Nari in cylindrical coordinates (r, λ, z), where r is the radius from the TC center pointing outward, λ is the azimuthal angle, and z is the vertical height axis. While Nari is over ocean, the TC center is defined as the center of minimum sea level pressure; while Nari is over Taiwan island, the TC center is defined as the primary vortex circulation center at 4-km altitude (above the highest peak of Mt. Snow).

As in Braun (2006), the governing equation for water vapor q_v in a TC-following framework can be written as

$$\frac{\partial q_v}{\partial t} = -\nabla \cdot (q_v \mathbf{V}') - \frac{\partial (q_v w)}{\partial z} + q_v \left(\nabla \cdot \mathbf{V}' + \frac{\partial w}{\partial z} \right)$$
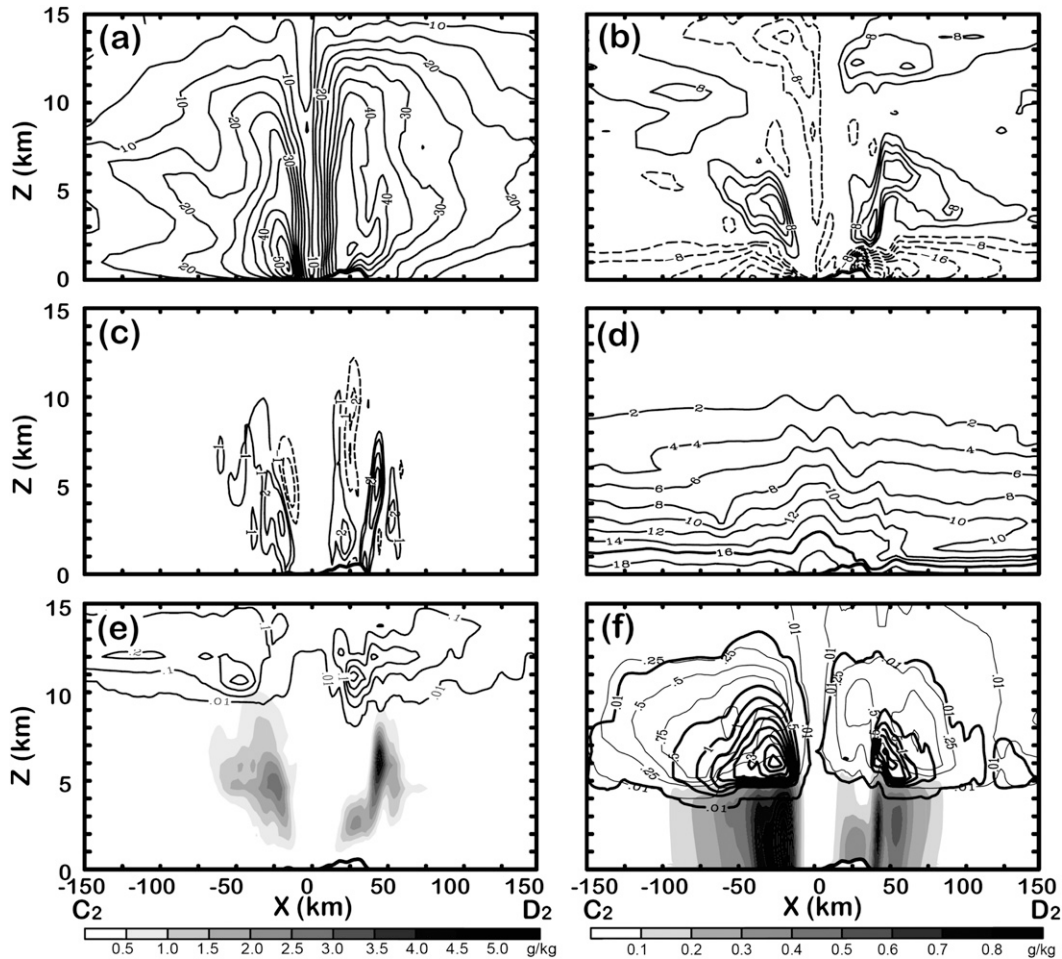$$- C + E + B_v + D_v + \text{Resd}_v. \quad (1)$$

FIG. 6. As in Fig. 5 but for C_2D_2 vertical cross section.

Similarly, the equation for cloud ($q_c = q_l + q_i$) can be written as

$$\frac{\partial q_c}{\partial t} = -\nabla \cdot (q_c \mathbf{V}') - \frac{\partial (q_c w)}{\partial z} + q_c \left(\nabla \cdot \mathbf{V}' + \frac{\partial w}{\partial z} \right)$$
$$+ Q_{c+} - Q_{c-} + B_c + D_c + \text{Resd}_c, \qquad (2)$$

and the equation for precipitation ($q_p = q_r + q_s + q_g$) can be written as

$$\frac{\partial q_p}{\partial t} = -\nabla \cdot (q_p \mathbf{V}') - \frac{\partial (q_p w)}{\partial z} + q_p \left(\nabla \cdot \mathbf{V}' + \frac{\partial w}{\partial z} \right)$$
$$+ \frac{\partial (q_p V_T)}{\partial z} + Q_{p+} - Q_{p-} + D_p + \text{Resd}_p, \qquad (3)$$

where q_v, q_c, and q_p are the water vapor, cloud, and precipitation mixing ratios, respectively; $\mathbf{V}'$ is the storm-relative horizontal air motion; w and V_T are the vertical

air and hydrometeor terminal velocities, respectively; Q_{c+}, Q_{c-}, Q_{p+}, and Q_{p-} are the cloud and precipitation microphysical source ($+$) and sink ($-$) terms; C is the condensation and deposition; E is the evaporation and sublimation. We have

$$C - E = Q_{c+} - Q_{c-} + Q_{p+} - Q_{p-}.$$

The B_v and B_c are the contributions from the planetary boundary layer parameterization and vertical turbulent diffusion to the vapor and cloud budgets, respectively; and D_v, D_c, and D_p are numerical diffusion terms for vapor, cloud, and precipitation, respectively. Microphysical source and sink terms are output directly from the Reisner et al. (1998) microphysical parameterization code. The Resd_v, Resd_c, and Resd_p terms are the residual terms of the vapor, cloud, and precipitation budgets, respectively, due to numerical errors in the model finite-difference formulation (including the spatial central-differencing error, temporal leapfrog-differencing error, interpolation

error, and errors from setting negative mixing ratios to zero). So residual terms in this study are different from the "zero" terms in Braun (2006), which specifically represent the artificial source terms associated with setting negative mixing ratios to zero. The first two terms on the right-hand side of Eqs. (1)–(3) are the horizontal and vertical flux convergence terms (including the minus sign), so a flux convergence (divergence) creates a positive (negative) change in the respective mixing ratio field. The third term on the right-hand side of Eqs. (1)–(3) is the change in the mixing ratio field due to the three-dimensional airflow divergence following the storm motion. Each term in Eqs. (1)–(3) except for the residual term is output directly from MM5. Parameter names and mathematical formulations of budget terms are given in Table 1.

While performing the water budget calculations, several definitions of averages are used as in Braun (2006). First, the temporal and azimuthal mean is defined as

$$\overline{[\ ]} = \frac{1}{2\pi(T_2 - T_1)}\int_{T_1}^{T_2}\int_0^{2\pi}\rho[\ ]\,\partial\lambda\,\partial t, \qquad (4)$$

the time-averaged and vertically integrated amount is defined as

$$[\hat{\ }] = \frac{1}{(T_2 - T_1)}\int_{T_1}^{T_2}\int_{Z_B}^{Z_T}\rho[\ ]\,\partial z\,\partial t, \qquad (5)$$

and the time-averaged, volumetrically integrated amount is defined as

$$\overline{\overline{[\ ]}} = \int_{Z_B}^{Z_T}\int_{R_1}^{R_2}\overline{[\ ]}2\pi r\,\partial r\,\partial z, \qquad (6)$$

where T_1 and T_2 are the beginning and ending times for the analysis (13 and 14 h while Nari is over ocean; 23.5 and 24.5 h while Nari is over land); Z_B and Z_T are the heights of the lowest and uppermost half-σ levels of the model domain; and R_1 and R_2 are the radial limits of integration. The typhoon circulation of Nari can be separated into two distinct components: the inner core ($R = $ 0–50 km) including the eye and eyewall, and the outer-rainband region ($R = $ 50–150 km) including the rainbands and stratiform precipitation area (see Fig. 1). Thus R_1 and R_2 are 0 and 50 km for the inner core and 50 and 150 km for the outer region, respectively.

The units of the quantities derived from Eqs. (4)–(6) are kg m^{-3} h^{-1}, kg m^{-2} h^{-1}, and kg h^{-1}, respectively. Each water budget term in Eqs. (1)–(3) is averaged using Eq. (6) from $R = 0$ to $R = 50$ km for the inner-core region, and from $R = 50$ km to $R = 150$ km for the outer-rainband region. All values are then normalized by the storm-total condensation between $R = 0$ and $R = 150$ km and then multiplied by 100. All calculated water budget terms (with definitions given in Table 1) are discussed in

TABLE 1. Water budget parameter names.

Name	Term	Description/comment
Cond	$\overline{\overline{C}}$	Condensation and deposition
Evap	$\overline{\overline{E}}$	Evaporation and sublimation
HFP	$\overline{-\mathbf{V}\cdot(q_x\mathbf{V}')} > 0$	Inward-directed (positive) horizontal flux convergence
HFN	$\overline{-\mathbf{V}\cdot(q_x\mathbf{V}')} < 0$	Outward-directed (negative) horizontal flux convergence
HFC	HFP + HFN	Net horizontal flux convergence
VFP	$-\overline{\overline{\dfrac{\partial(q_x w)}{\partial z}}} > 0$	Positive vertical flux convergence
VFC	$-\overline{\overline{\dfrac{\partial(q_x w)}{\partial z}}}$	Vertical flux convergence
Div	$\overline{\overline{q_x\left(\mathbf{V}\cdot\mathbf{V}' + \dfrac{\partial w}{\partial z}\right)}}$	Divergence term
P	$\overline{\overline{\dfrac{\partial(q_p V_T)}{\partial z}}}$	Precipitation flux
Diff	$\overline{\overline{D_x}}$	Numerical diffusion
PBL	$\overline{\overline{B_x}}$	Boundary layer source and vertical (turbulent) diffusion
Tend	$\overline{\overline{\dfrac{\partial q_x}{\partial t}}}$	Storage term
Resd	$\overline{\overline{\mathrm{Resd}_x}}$	Residual term

the next section. Thus for each analyzed region (inner-core or outer-rainband region), the water vapor budget described in Eq. (1) can be expressed using the budget terms defined in Table 1 as

$$\begin{aligned}\text{Tend} = {}& \text{Cond} + \text{Evap} + \text{HFC} + \text{VFC} + \text{Div} \\ & + \text{Diff} + \text{PBL} + \text{Resd}.\end{aligned} \qquad (7)$$

Similarly, the water condensate (cloud and precipitation) budget described by combining Eqs. (2) and (3) can be expressed using the budget terms defined in Table 1 for each region as

$$\begin{aligned}\text{Tend} = {}& \text{Cond} + \text{Evap} + \text{HFC} + \text{VFC} + \text{Div} \\ & + \text{Diff} + \text{PBL} + \text{P} + \text{Resd}.\end{aligned} \qquad (8)$$

4. Result

a. Water vapor budget

Figure 7 shows the azimuthally and temporally (13–14 h) averaged water vapor budget terms while Nari was still over ocean. Condensation and deposition [C in Eq. (1)] are the major sinks of water vapor, and evaporation and sublimation [E in Eq. (1)] are the major sources of water vapor. Most of the condensation occurs within the eyewall, within areas of mesoscale updrafts in outer
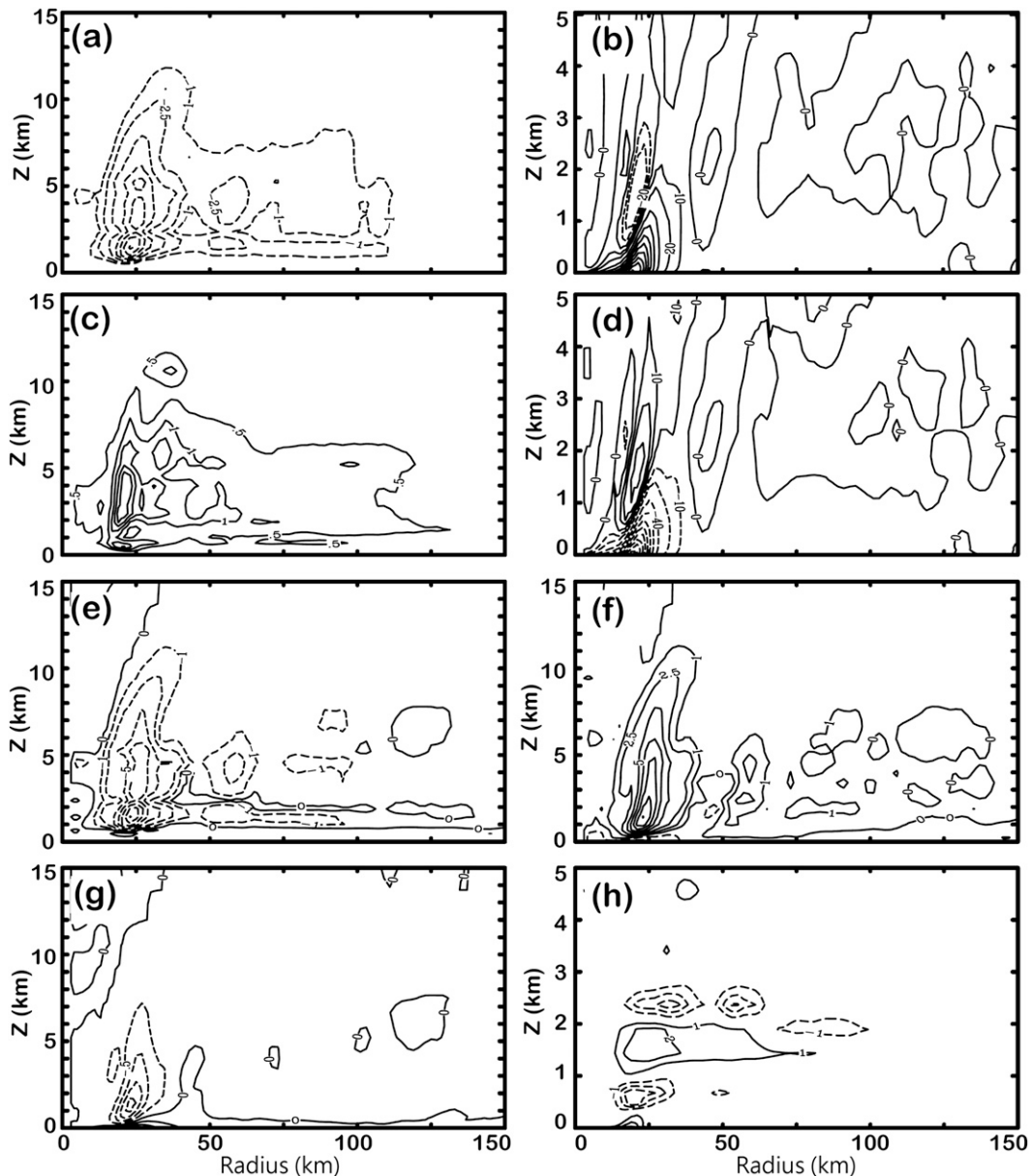
FIG. 7. Azimuthally and temporally (13–14 h) averaged water vapor budget fields of (a) condensation (plus deposition), (b) horizontal flux convergence, (c) evaporation (plus sublimation), (d) vertical flux convergence, (e) net condensation [sum of (a) and (c)], (f) total flux convergence [sum of (b) and (d)], (g) divergence term, and (h) boundary layer source and vertical diffusion term. Contour values in (a),(e), and (f) are at 2.5 g m^{-3} h^{-1} intervals, with extra contours at ± 1 g m^{-3} h^{-1}. Contour values in (b) and (d) are at 20 g m^{-3} h^{-1} intervals, with extra contours at ± 10 g m^{-3} h^{-1}. Contour values in (c) and (g) are at 0.5 g m^{-3} h^{-1} intervals. Contour values in (h) are 1 g m^{-3} h^{-1}. In (b),(d), and (h), only the lowest 5 km are shown to improve readability since values above these levels are generally small. Solid (dashed) lines indicate positive (negative) values.

rainbands, and near the top of the boundary layer (Fig. 7a). Evaporation of cloud and rain occurs mostly along the inner edge of the eyewall, in outer rainbands, near the top of the boundary layer, and near the melting layer at $z = 5$ km (Fig. 7c). The net microphysical sink term for water vapor [$C–E$ in Eq. (1)] is shown in Fig. 7e, and indicates

the net loss of water vapor by net condensation and deposition within the eyewall and outer rainbands.

Because of the highly incompressible nature of air motion, the horizontal vapor flux convergence is nearly out of phase with the vertical vapor flux convergence (Figs. 7b,d). In other words, the strong low-level radial

inflow transports highly moist air parcels from the surrounding oceanic environment inward to the eyewall (Figs. 3b, 7b), and then the deep updrafts within the eyewall transport the moisture upward (Figs. 3c, 7d). The total vapor flux convergence in Fig. 7f, which is the summation of the horizontal and vertical vapor flux convergences, is largely compensated by the net microphysical sink term [$C–E$ in Eq. (1)] in Fig. 7e. The near balance between the total vapor flux convergence and net microphysical sink results in a very small vapor tendency (not shown). The divergence term shows horizontal flow convergence within the boundary layer and vertical flow divergence within the eyewall (Fig. 7g). The boundary layer parameterization and vertical diffusion produce oscillations of small positive and negative changes of vapor in the lowest 3 km (Fig. 7h).

After Nari's landfall on Taiwan, asymmetric features of the vapor budget are different from the axisymmetric structures over the ocean. Figure 8 displays the temporally averaged (23.5–24.5 h) water vapor budget fields along the A_2B_2 vertical cross section. Condensation maxima are within the northeastern eyewall near the coast and in the updrafts along the mountain slopes (Figs. 5c, 8a). On the other hand, evaporation occurs mainly within the downdrafts over the mountain area (Figs. 5c, 8c), although its peak magnitude is much weaker than that of condensation. By adding these two terms together, net condensation yields a net loss of vapor within the coastal eyewall and a net loss of vapor within the updrafts and a net gain of vapor within the downdrafts over the mountain area (Fig. 8e). Because of enhanced flow convergence and divergence after the storm's landfall, vapor flux convergence over land (Figs. 8b,d) is stronger than that over ocean (Figs. 7b,d; note the contour interval differences between Figs. 7b,d and 8b,d). Again, horizontal vapor flux convergence is out of phase with vertical vapor flux convergence (Figs. 8b,d). Total vapor flux convergence is again opposite in sign to the net condensation (Figs. 8e,f), consistent with the axisymmetric results over the ocean (Figs. 7e,f). Vapor change due to flow divergence over land produces the loss and gain of water vapor below 5 km (Fig. 8g). Boundary layer processes and vertical diffusion produce enhanced positive and negative changes of water vapor over the rugged terrain (Fig. 8h), compared to those over the ocean (Fig. 7h).

b. Condensed water budget

Figure 9 displays the azimuthally and temporally (13–14 h) averaged budget terms of condensed water (cloud and precipitation) for the period over ocean. The net source of condensed water in Fig. 9a, which is the summation of net condensation and evaporation [$C–E$ in Eq. (1)], is opposite in sign to the net sink of water vapor in Fig. 7e. Again, because air motion is nearly incompressible, the horizontal flux convergence of condensed water is out of phase with the vertical flux convergence (Figs. 9b,d). The precipitation fallout term indicates a large fallout of raindrops and graupel particles inside the eyewall (Fig. 9c). Fallout outside of the eyewall is enhanced across the melting layer and in the locations of large rain and graupel mixing ratios in the outer rainbands (Figs. 3f, 9c). The boundary layer parameterization and vertical diffusion produce oscillations of positive and negative changes of cloud and precipitation in the lowest 3 km (Fig. 9e). Summation of precipitation fallout and total flux convergence (Fig. 9f) is mostly out of phase with the net source term of condensed water (Fig. 9a), indicating that the condensed water is falling out as rapidly as it is produced during the over-ocean stage.

Sources and sinks of rain, graupel, and snow are shown in Fig. 10. The collocation between the rain source (Fig. 10a) and graupel sink (Fig. 10d) near the melting layer ($z = 5$ km) indicates that the melting of graupel particles contributes significantly to the production of raindrops. Collision and coalescence of cloud droplets accounts for the rain production beneath the melting layer within the eyewall (Fig. 10a), and collection of raindrops by snowflakes occurs in the mid-to-upper levels (Fig. 10b). The maximum of the graupel source is located at a lower height than that of the snow source (Figs. 10c,e), owing to the larger fall speeds of graupel particles. Melting of snowflakes also produces raindrops (Fig. 10f), although this rain production is much less than that from the melting of graupel particles (Fig. 10d). Although there was no in situ microphysics observation for Typhoon Nari, observational studies of Black and Hallett (1986) for Hurricane Irene (1981), Houze et al. (1992) for Hurricane Nobert (1984), and McFarquhar and Black (2004) for Hurricane Emily (1987) all indicated a strong association between large raindrops and the melting of graupel particles. Thus, it is possible that graupel melting could contribute significantly to heavy rainfall in Typhoon Nari.

There are some noticeable differences in the rain source–sink terms between this study using the Reisner et al. (1998) scheme and the study of Braun (2006) using the Goddard microphysics scheme (Tao and Simpson 1993). The rain source term (mainly the accretion of supercooled cloud droplets by raindrops and the autoconversion of cloud droplets to raindrops) in Fig. 10a extends to higher levels above the melting level, compared to that in Braun (2006, see his Fig. 9a), mainly due to the assumed availability of abundant supercooled cloud droplets at midlevels (5–10 km) in the Reisner et al. scheme. Also, the rain sink term in Fig. 10b is much weaker than that in Braun (2006, see his Fig. 9b) below
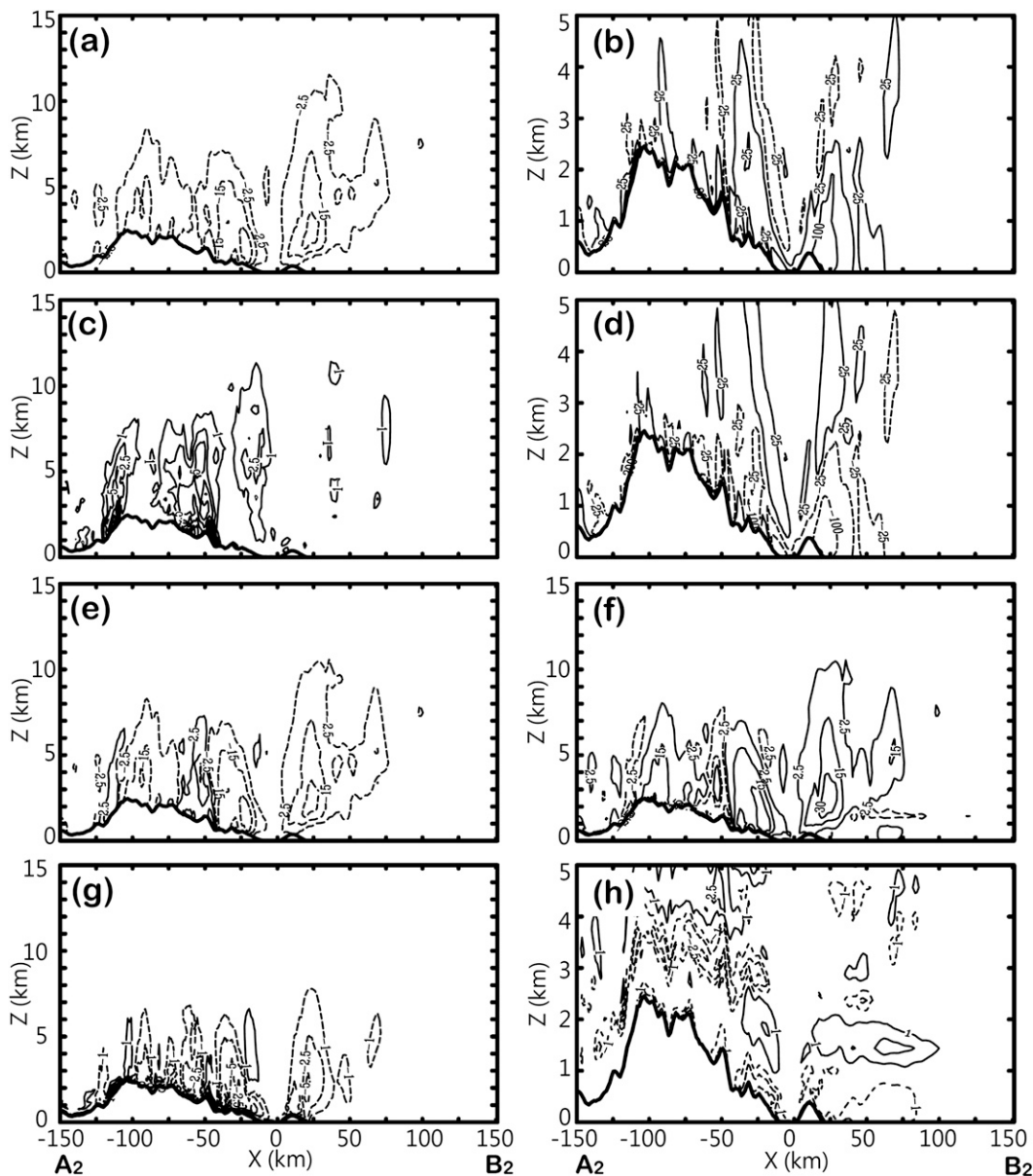
FIG. 8. As in Fig. 7 but for the A_2B_2 vertical cross section of temporally (23.5–24.5 h) averaged fields. Contour values in (a),(e), and (f) are at 15 g m^{-3} h^{-1} intervals, with extra contours at ±2.5 g m^{-3} h^{-1}. Contour values in (b) and (d) are at -100, -25, 25, and 100 g m^{-3} h^{-1}. Contour values in (c),(g), and (h) are at 2.5 g m^{-3} h^{-1} intervals, with extra contours at ±1 g m^{-3} h^{-1}. In (b),(d), and (h), only the lowest 5 km are shown to improve readability since values above these levels are generally small. Solid (dashed) lines indicate positive (negative) values.

the melting level, probably because of a much moister environment for Nari than for Bonnie.

The temporally (23.5–24.5 h) averaged cloud and precipitation budget fields during the landfall stage along the A_2B_2 cross section are shown in Fig. 11 and are consistent with characteristics during the over-ocean stage. The net microphysical source (Fig. 11a) corresponds well to the time-averaged cloud (Fig. 5e) and rainwater (Fig. 5f) mixing ratios. The precipitation fallout (Fig. 11c) resembles

closely the mixing ratio fields of graupel and rain (Fig. 5f). Horizontal flux convergence (Fig. 11b) is stronger than (but of opposite sign to) vertical flux convergence (Fig. 11d). The boundary layer source and vertical diffusion term are very small (not shown). Precipitation fallout and total flux convergence (Fig. 11e) are largely opposite in sign to the net microphysical source (Fig. 11a), implying that a net balance exists between the generation of cloud and precipitation and their loss.
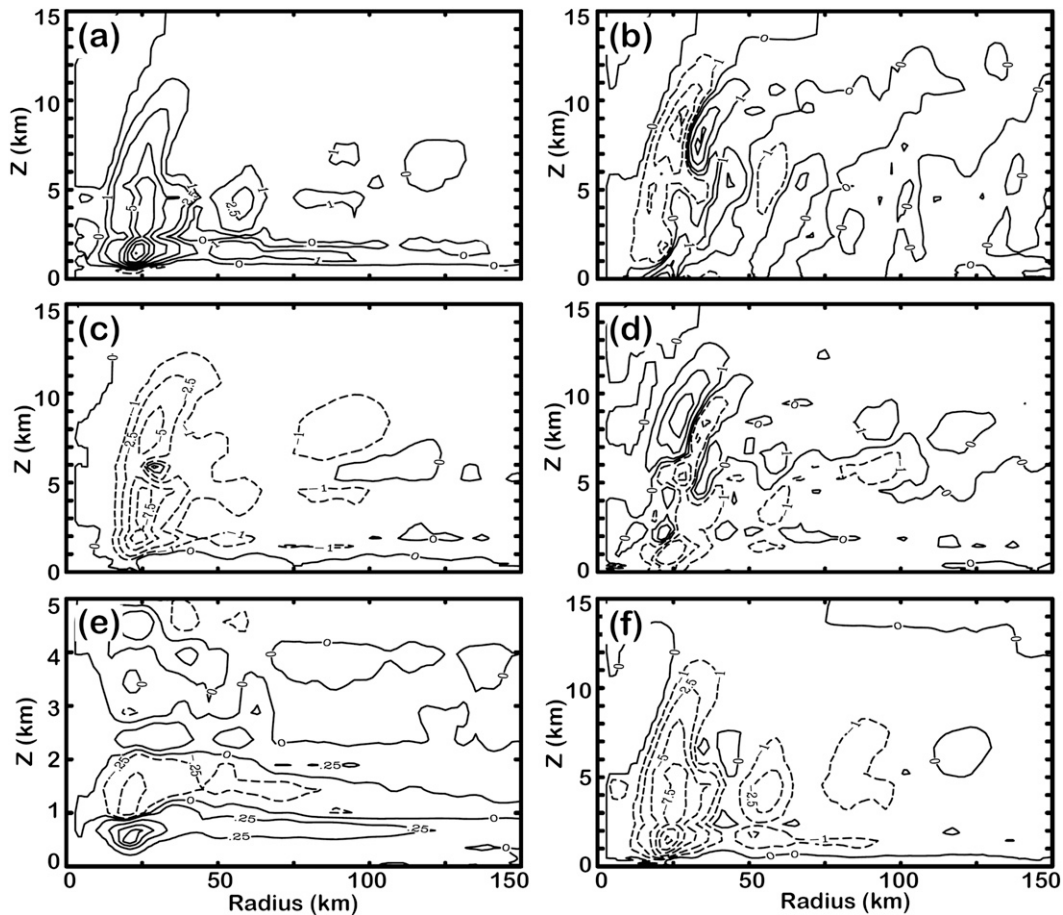
FIG. 9. Azimuthally and temporally (13–14 h) averaged cloud and precipitation budget fields of (a) net source (condensation, deposition, evaporation, and sublimation), (b) horizontal flux convergence, (c) precipitation fallout, (d) vertical flux convergence, (e) boundary layer source term, and (f) precipitation fallout and total flux convergence [sum of (b),(c), and (d)]. Contour values in (a),(c), and (f) are at 2.5 g m^{-3} h^{-1} intervals, with extra contours at ± 1 g m^{-3} h^{-1}. Contour values in (e) are 1 g m^{-3} h^{-1} intervals, with extra contours at ± 0.25 g m^{-3} h^{-1}. Contour values in (b) and (d) are at ± 10, ± 5, ± 3, ± 1, and 0 g m^{-3} h^{-1}. Solid (dashed) lines indicate positive (negative) values.

c. Vertically integrated sources and sinks

The vertically integrated and time-averaged source terms for total rain, warm rain, and cold rain during the over-ocean and landfall stages, respectively, of Nari are shown in Fig. 12. During the oceanic stage, warm rain processes dominate in the eyewall region (Fig. 12b), while cold rain processes (mainly the melting of graupel particles to produce raindrops) are comparable to the warm rain processes outside of the eyewall (Fig. 12c). After landfall, the total rain source is significantly increased by the enhanced moisture convergence over the northwestern coast and orographic lifting above the northern CMR (Fig. 12d). Warm rain processes increase and still dominate in the eyewall region after landfall (Fig. 12e); above the northern CMR, cold rain processes are enhanced

(Fig. 12f), resulting in increased rainfall over the terrain by the melting of graupel particles (Fig. 5f).

The vertically integrated and time-averaged source terms of condensation, evaporation, and precipitation fallout during the oceanic and landfall stages, respectively, are shown in Fig. 13. When the storm is over ocean, intense condensation occurs within the eyewall, and weaker condensation and deposition are in the principal rainband (Fig. 13a). Evaporation and sublimation are weaker, but occur over regions much wider than the inner core and outer rainbands, including the surrounding subsaturated areas (Fig. 13b). The horizontal distribution of the precipitation fallout term (Fig. 13c) corresponds well to the simulated radar reflectivity field (see the color shading in Figs. 1a–c). After the storm's landfall, peak values of condensation and evaporation are much stronger
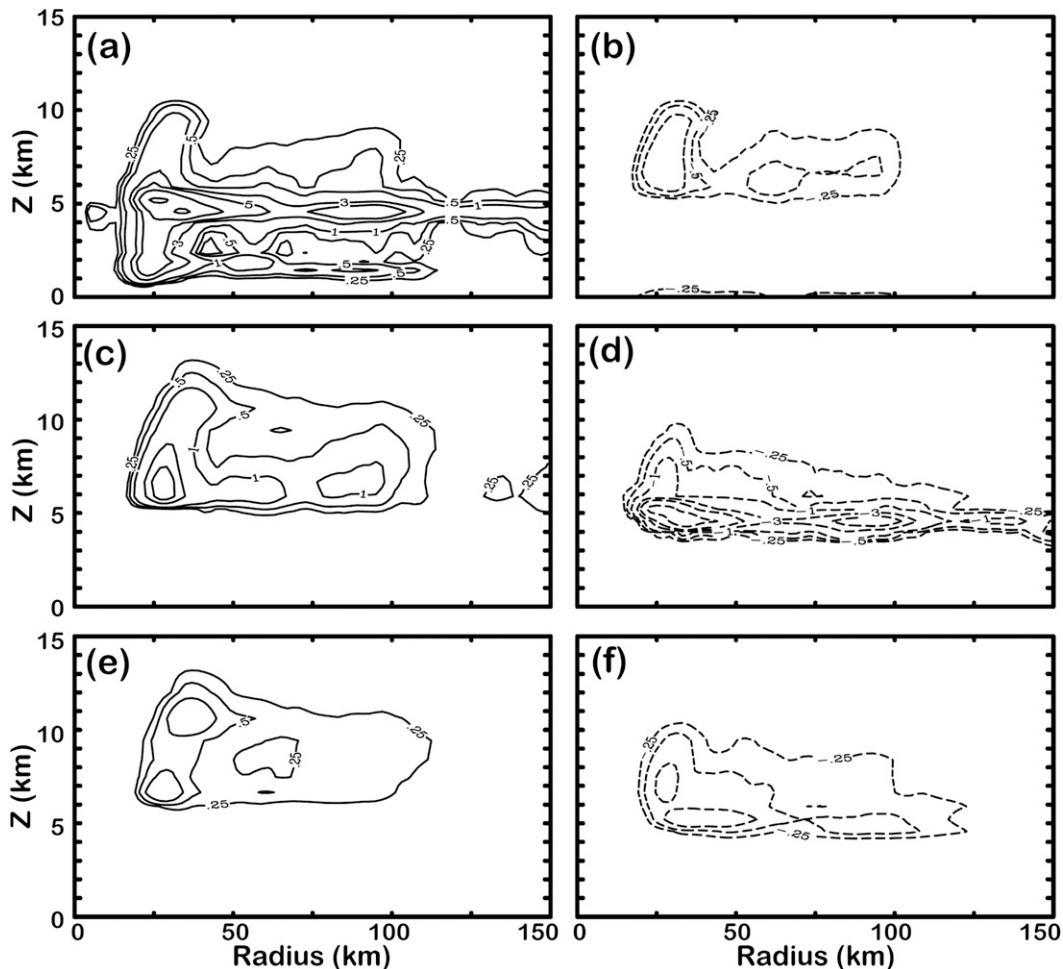
FIG. 10. Azimuthally and temporally (13–14 h) averaged precipitation source terms showing (a),(c),(e) sources and (b),(d),(f) sinks for rain, graupel, and snow, respectively. Contour values are at ± 20, ± 10, ± 5, ± 3, ± 1, ± 0.5, and ± 0.25 g m^{-3} h^{-1}. Solid (dashed) lines indicate positive (negative) values.

(by 2–4 times) than those prior to landfall (Figs. 13d,e), corresponding to enhanced precipitation fallout (Fig. 13f) and stronger radar echoes (Figs. 4b,c) on the northwestern side of the island.

d. Volume-integrated budgets

Figure 14 displays diagrams of the volume-integrated water vapor budget terms in the two 1-h periods: the over-ocean period of 13–14 h and the landfall period of 23.5–24.5 h. The two blocks in each diagram indicate the inner-core area ($r < 50$ km) and the outer-rainband region (50 km $< r <$ 150 km). After Nari's landfall, the storm-total condensation within a 150-km radius is increased from 7.41×10^{11} kg h^{-1} to 9.06×10^{11} kg h^{-1}, approximately a 22% enhancement. When Nari is still over the ocean, the vapor source from the underlying ocean in the inner core is only 5.5% (1.3/23.5) of the inward vapor flux across the eyewall; over the outer-rainband region, evaporation from the ocean is 15% (4.7/31.3) of the horizontal convergence of the inward vapor flux from the surrounding environment beyond a 150-km radius. In other words, the ocean vapor source within the 150-km radius from the storm center is 10.9% [(1.3 + 4.7)/(23.5 + 31.3)] of the inward vapor transport. This finding supports previous estimates, which indicate that the ocean vapor source is only a small percentage of the total water vapor import, consistent with previous studies in Malkus and Riehl (1960), Kurihara (1975), and Braun (2006). For the whole storm within 150 km from the center, the net horizontal vapor convergence (46.9% = 31.3% + 23.5% − 2.3% − 5.6%) into the storm is 87.8% (46.9/53.4) of the net condensation (53.4% = 32.4% + 67.6% − 10.5% − 36.1%), indicating the high efficiency of the horizontal vapor transport to supply nearly all of the net condensation. After Nari's landfall, the boundary layer vapor source decreases significantly because of the
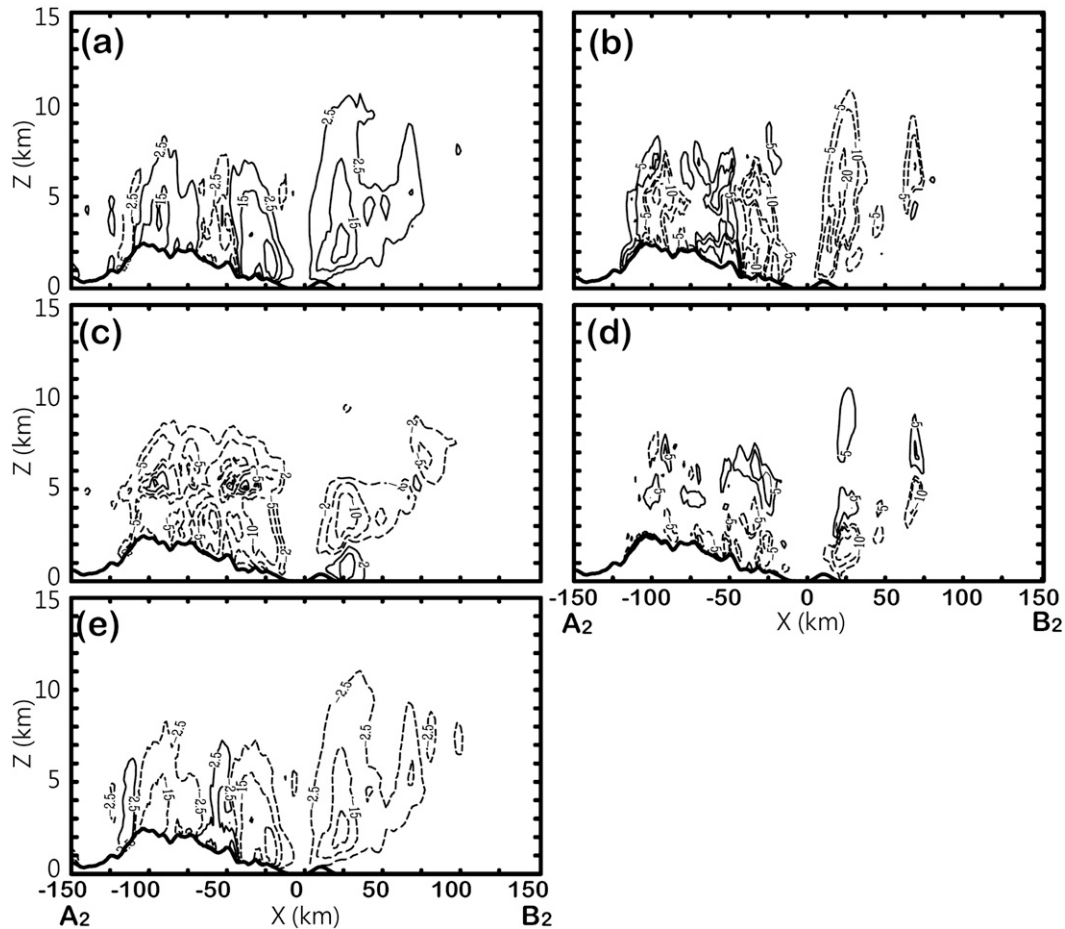
FIG. 11. The A_2B_2 vertical cross section of temporally (23.5–24.5 h) averaged cloud and precipitation budget fields of (a) net source (condensation, deposition, evaporation, and sublimation), (b) horizontal flux convergence, (c) precipitation fallout, (d) vertical flux convergence, and (e) precipitation fallout and total flux convergence [sum of (b),(c), and (d)]. Contour values in (a) and (e) are at 15 g m^{-3} h^{-1} intervals, with extra contours at ±2.5 g m^{-3} h^{-1}. Contour values in (b) and (d) are at ±50, ±20, ±10, and ±5 g m^{-3} h^{-1}. Contour values in (c) are at ±20, ±10, ±5, and ±2 g m^{-3} h^{-1} intervals.

reduced moisture fluxes over the rugged terrain (0.1% versus 1.3% over the inner core; 2.3% versus 4.7% over the outer region).

Condensation within the inner core accounts for 32.4% of the storm-total condensation for the oceanic stage, but increases to 48.0% of the total condensation during the landfall stage, which is consistent with the enhanced convection and precipitation within the inner core right after Nari's landfall. The low-level inward vapor flux convergence (HFP) and upper-level outward vapor flux divergence (HFN) for the inner-core region are significantly increased after landfall. To be specific, the inward (outward) vapor transport across the inner-core boundary at the lower (upper) levels is increased by more than 3 times (10 times) after landfall (72.6% versus 23.5% for HFP at low levels; 26.4% versus 2.3% for HFN at upper levels). This result occurs because the lower-level (upper

level) radial inflow (outflow) is deeper and stronger with more moist air after landfall (Figs. 5b,d). Because of the enhanced low-level convergence and upper-level divergence after landfall, the net horizontal vapor convergence (80.6% = 40.2% + 72.6% − 26.4% − 5.8%) into the storm within the 150-km radius is 122.3% (80.6/65.9) of the net condensation (65.9% = 48.0% + 52.0% − 10.6% − 23.5%) after landfall.

Figure 15 shows the corresponding total condensate (cloud and precipitation) budget for Nari prior to and after landfall. Surface precipitation within the inner core accounts for 23.6% of the storm-total condensation over the ocean, but increases to 32.2% over land. This precipitating portion is similar to the net condensation (32.4% − 10.5% = 21.9% over ocean; 48.0% − 10.6% = 37.4% over land), implying that water condensate is precipitated out as quickly as it is produced in situ (Braun
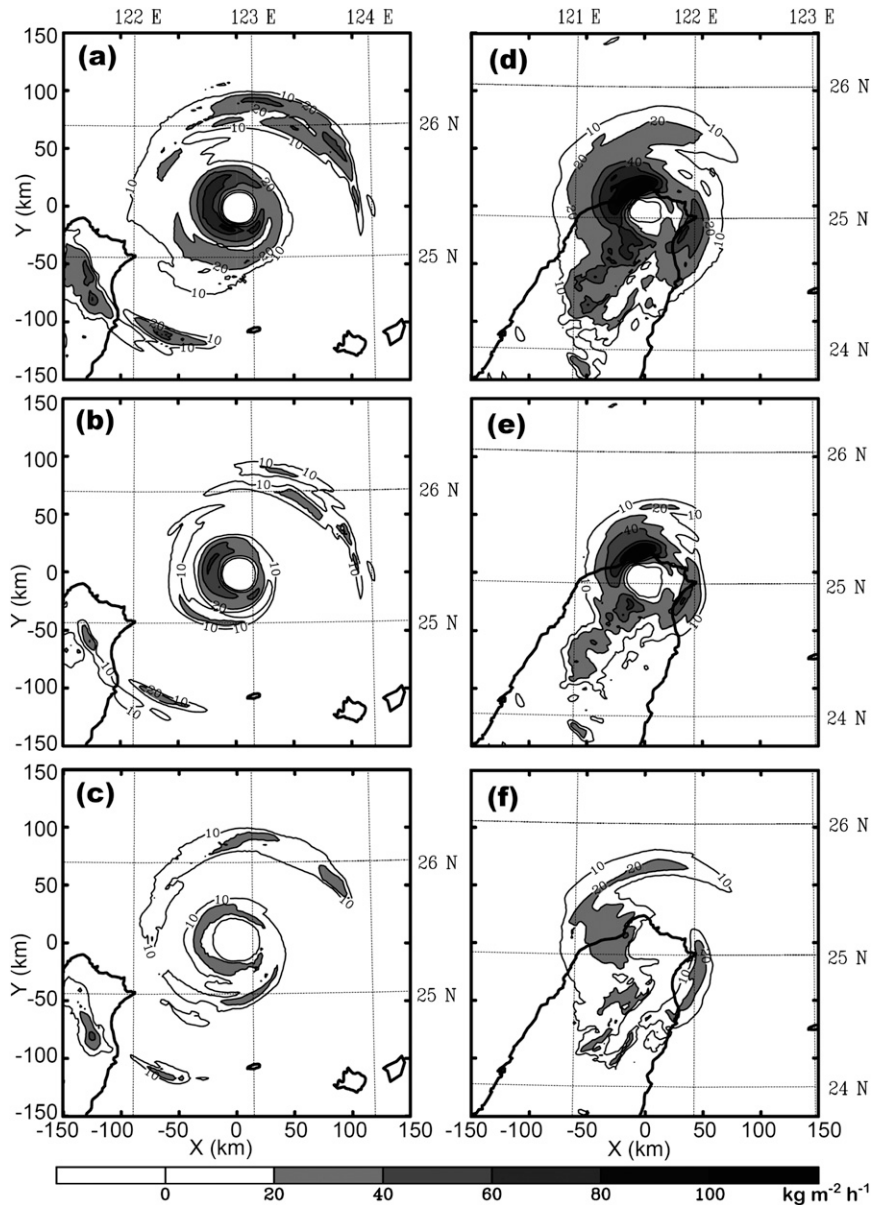
FIG. 12. Vertically integrated and time-averaged source terms for (a),(d) total rain source, (b),(e) warm rain source, and (c),(f) cold rain source. Panels (a)–(c) are for source terms averaged at 13–14 h and (d)–(f) are for source terms averaged at 23.5–24.5 h. Contour values are at 20 kg m^{-2} h^{-1} intervals, with extra contours at 10 kg m^{-2} h^{-1}.

2006). The HFP and HFN are increased after landfall, again because the storm's secondary circulation is stronger after landfall (Figs. 5b,c). Note that the HFN of condensate from the inner core to the outer region is quite small (1.2% over ocean and 9.2% over land), probably because Typhoon Nari (2001) was only a category 2 on the Saffir–Simpson hurricane scale prior to landfall and then quickly weakened to tropical-storm strength after landfall on Taiwan (see Fig. 5 of YZH). The relatively weaker outflows of Nari at the upper level (only up to 6 m s^{-1} at 12 km; see

Fig. 3b) produce a smaller flux of water and ice from the eyewall to outer-rainband region, compared to other intense TCs with stronger storm intensities and stronger upper-level outflows.

e. Precipitation efficiencies

There are several ways to define and calculate the precipitation efficiency (Doswell et al. 1996; Ferrier et al. 1996; Li et al. 2002; Sui et al. 2005, 2007). One way is to define the efficiency from a microphysical perspective
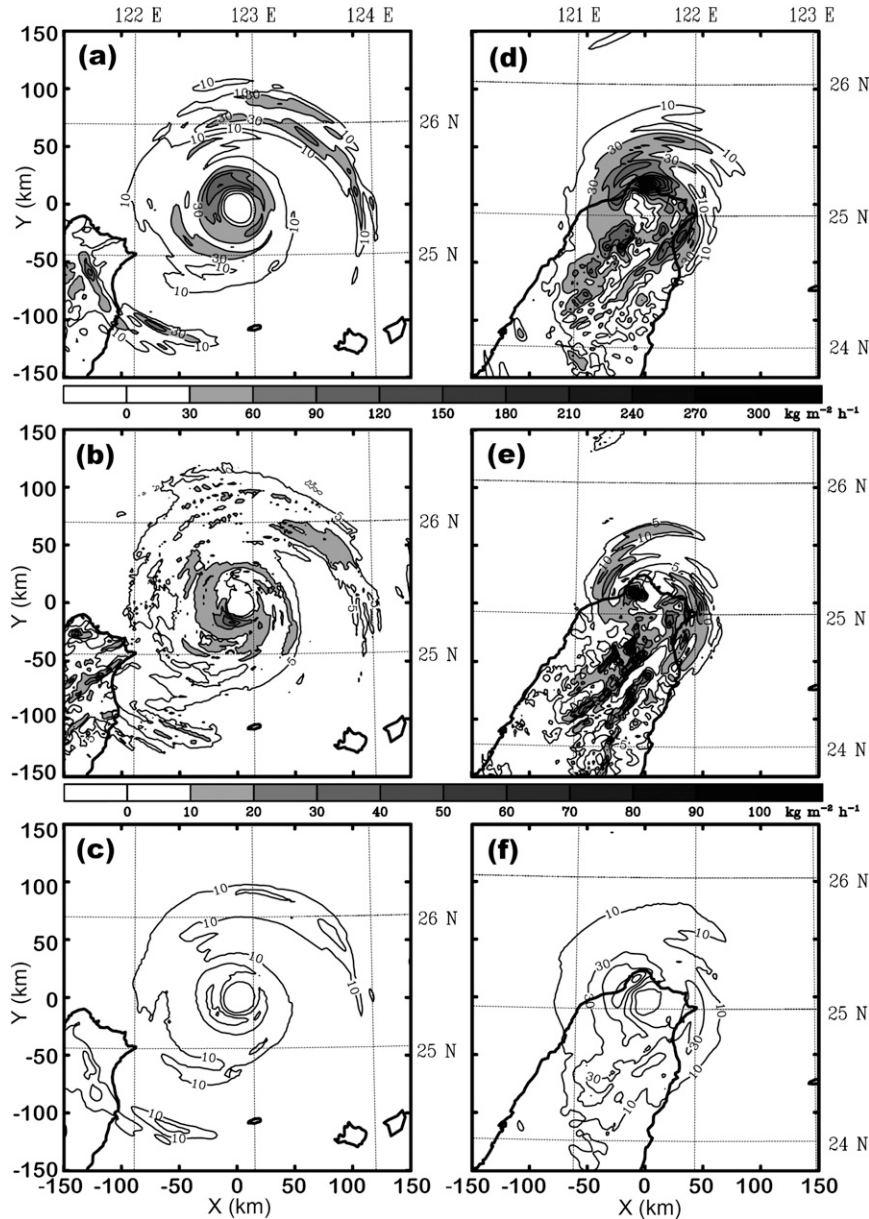
FIG. 13. As in Fig. 12 but for (a),(d) condensation plus deposition, (b),(e) evaporation plus sublimation, and (c),(f) precipitation fallout. Contour values in (a),(c),(d), and (f) are at 30 kg m^{-2} h^{-1} intervals, with extra contours at 10 kg m^{-2} h^{-1}. Contour values in (b) and (e) are at 10 kg m^{-2} h^{-1} intervals, with extra contours at 5 kg m^{-2} h^{-1}.

[the cloud microphysics precipitation efficiency (CMPE), i.e., the ratio of total precipitation with respect to total condensation]. Another more commonly used way is to define the efficiency from a large-scale vapor budget perspective [the large-scale precipitation efficiency (LSPE), i.e., the ratio of total precipitation with respect to total vapor transport into a large-scale area]. The LSPE can be directly calculated from the observation data within a sounding network; the CMPE, on the other hand, can

only be obtained from the output of a model. Sui et al. (2005, 2007) showed that these two efficiencies are equivalent if the averaging area is large enough or the averaging time period is long enough.

Using the budget terms defined in Table 1, the CMPE and LSPE can be calculated as

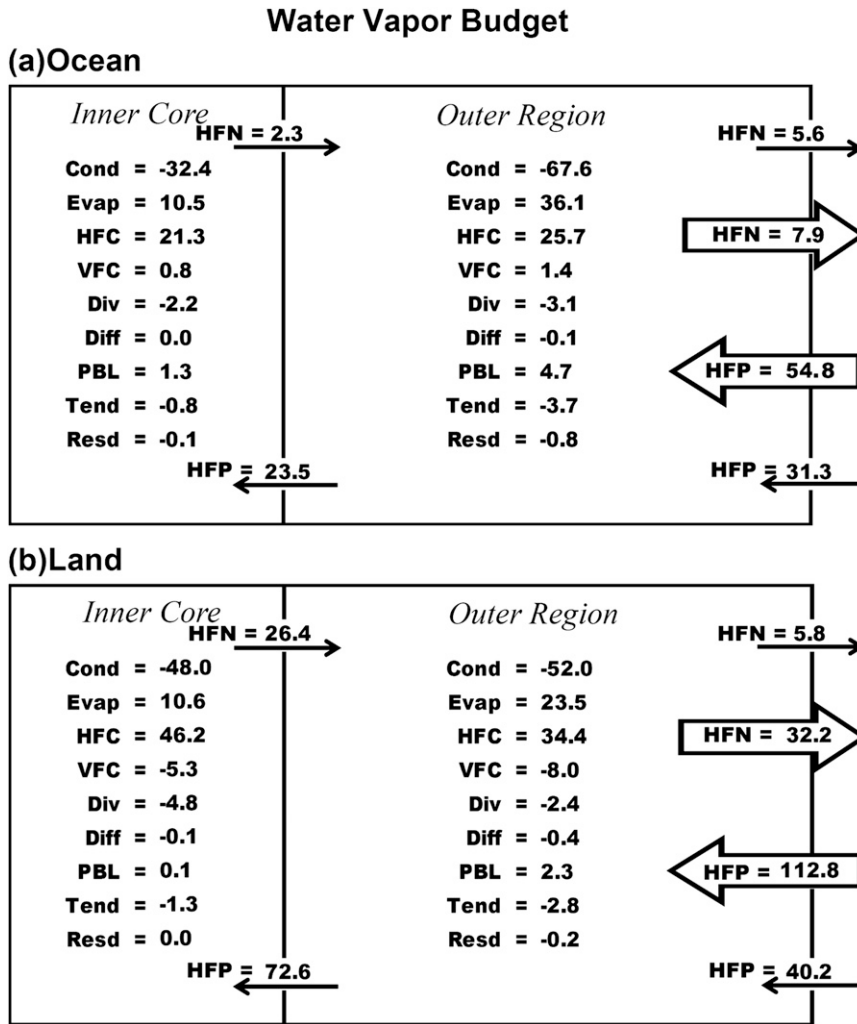$$\text{CMPE} = \frac{P}{\text{Cond}}, \tag{9}$$

FIG. 14. Water vapor budget over (a) ocean and (b) land. The lhs of the diagram represents the inner-core area (eye and eyewall, $r < 50$ km) while the rhs is for the outer region (50 km $< r < 150$ km). Parameter names are provided in Table 1. All values are normalized by the total condensation within $r < 150$ km. The nonnormalized values can be obtained by dividing by 100 and multiplying by the total condensation, which is 7.41×10^{11} kg h^{-1} over the ocean and 9.06×10^{11} kg h^{-1} over land, respectively. The inward (outward) thin arrow represents the HFP (HFN) to each region, and the inward (outward) open arrow represents the HFP (HFN) to the whole storm within a 150-km radius. The vapor balance in each region can be expressed by Eq. (7).

$$\text{LSPE} = \frac{P}{\text{HFP} + \text{VFP}}. \qquad (10)$$

Figure 16 displays the changes of CMPE and LSPE as a function of storm radius. Both efficiencies are increased over land for $r > 60$ km. In the inner core ($r < 50$ km), condensation is increased by a greater magnitude than precipitation after landfall (condensation is increased from 32.4% to 48.0% but precipitation is only increased from 23.6% to 32.2%; see Fig. 15), resulting in a smaller CMPE. At radii greater than 60 km, the CMPE remains at a constant value of 67% while Nari is over ocean and

73% while the storm is over Taiwan island. In general, the LSPE is about 10%–20% less than the CMPE except inside the eye ($r < 15$ km) where both efficiencies are very small, since the net inward vapor transport across the volume surface is much larger than the in situ production of net condensation inside the analysis volume. The reason why the CMPE remains roughly a constant value beyond the 60-km radius is not clear. One possible explanation is that outside of the inner-core precipitation region, stratiform precipitation dominates and has a fairly constant precipitation efficiency. More studies are required to investigate this issue further.
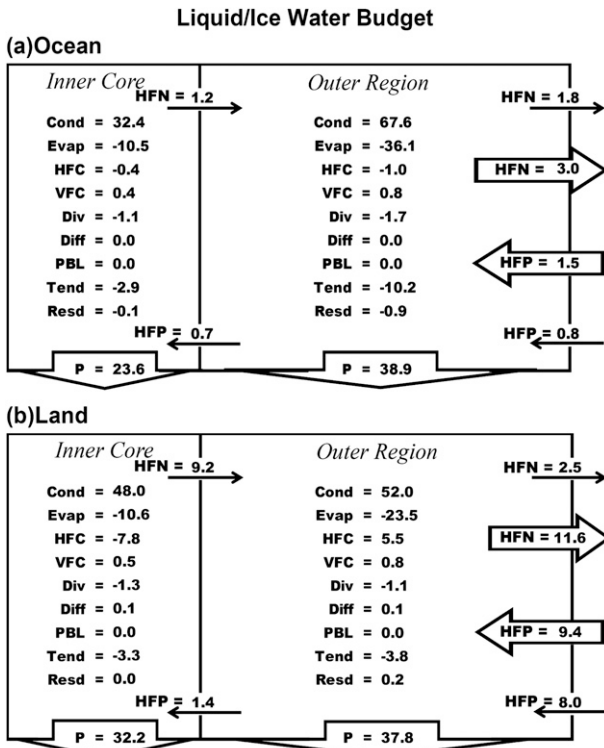
Liquid/Ice Water Budget

FIG. 15. As in Fig. 14 but for total condensate (cloud plus precipitation) budget over (a) ocean and (b) land. The water balance in each region can be expressed by Eq. (8).
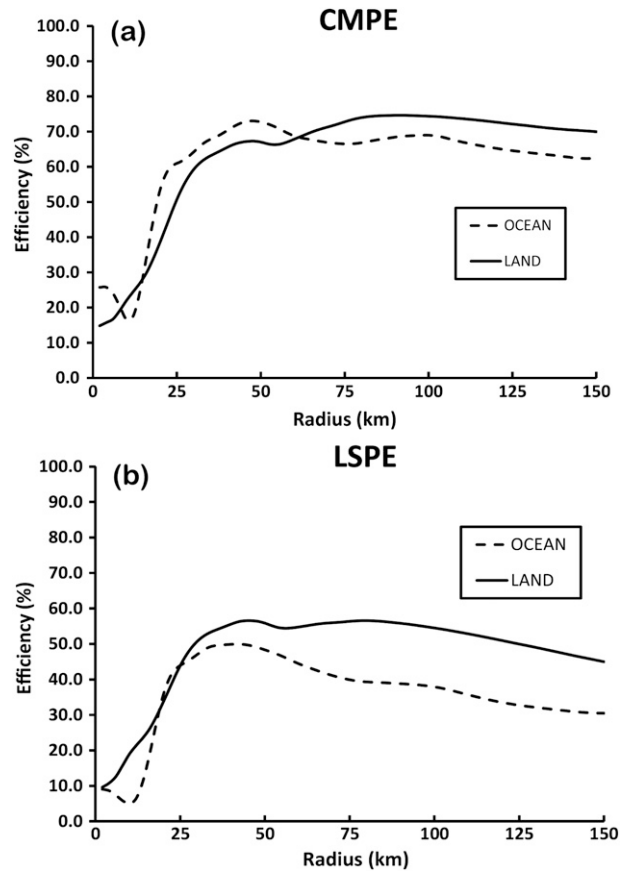

FIG. 16. Change of the (a) CMPE and (b) LSPE as a function of TC radius. Dashed line is for the time-averaged (13–14 h) result during the oceanic stage and solid line is for the time-averaged (23.5–24.5 h) result during the landfall stage.

5. Conclusions

In this study, high-resolution (2-km horizontal grid size and 2-min data interval) output from a cloud-resolving simulation of Typhoon Nari (2001) is used to examine the vapor and condensate budgets and the budget changes before and after Nari's landfall on Taiwan. All budget terms are directly derived from the model except for a small residual term. The storm circulation is divided into two parts, the inner-core and outer-rainband regions, respectively. To our knowledge, this study is the first one to examine the changes of TCs' vapor and water budgets from over ocean to landfall on the steep terrain and to discuss the increase of TCs' precipitation efficiency after landfall from the water budget perspective.

For the vapor budget, while Nari is over the ocean, evaporation from the ocean surface is 11% of the inward horizontal vapor transport within a 150-km radius from the storm center, and the net horizontal vapor convergence into the storm is 88% of the net condensation. The ocean source of water vapor in the inner core is a small portion (5.5%) of horizontal vapor import, consistent with previous studies. After landfall, Taiwan's steep terrain enhances Nari's secondary circulation significantly and results in stronger horizontal vapor import at lower levels

and more cloud ice and snow export to outer regions at upper levels across the inner core. Thus the net horizontal vapor convergence into the storm within 150 km is increased to 122% of the net condensation after landfall.

For the condensed water budget, summation of precipitation fallout and total flux convergence is largely out of phase with the net microphysical source term, indicating that precipitation particles are falling out as quickly as they are produced. Collision and coalescence of cloud droplets accounts for the major portion of the production of raindrops within the eyewall, while melting of graupel particles also contributes significantly to the production of raindrops. Thus, warm rain processes dominate in the eyewall region, while the cold rain processes are comparable to warm rain processes outside of the eyewall. After landfall, cold rain processes are further enhanced above the Taiwan terrain and the storm-total condensation within 150 km of the center is increased by 22%. In the eyewall, the low-level (upper level) inward (outward) vapor flux convergence (divergence) is increased by more than 3 times (10 times) after landfall, because the low-level

(upper level) radial inflow (outflow) is stronger and deeper with more moist air after the storm's landfall.

The exact magnitude of the water budget term may be sensitively dependent on the microphysics scheme used in the model. However, for the vapor budget, major balance exists between the total vapor flux convergence and the net vapor loss by net condensation and deposition. Similarly for the water condensate budget, total flux convergence of water condensate and precipitation fallout are mainly compensated by the net source of condensed water.

Precipitation efficiency, defined from either the large-scale or microphysics perspective, is increased 10%–20% over the outer-rainband region after landfall, in agreement with the enhanced surface rainfall over terrain. At radii greater than 60 km, the cloud microphysics precipitation efficiency remains at a constant value of 67% for the oceanic stage of Nari and 73% for the landfall stage. The reason why the precipitation efficiency remains roughly constant at these radii is not clear. One possible explanation is that the region outside of the eyewall is dominated by stratiform precipitation with a relatively constant precipitation efficiency. Further investigation on this issue is required in future studies.

It should be mentioned that the above conclusions are obtained by budget calculations of a tropical cyclone case from a numerical simulation in which some model deficiencies and physics uncertainties still exist. More water budget studies for landfall tropical cyclones over steep terrain are required in the future to generalize the results found in this study.

REFERENCES

Black, R. A., and J. Hallett, 1986: Observations of the distribution of ice in hurricanes. *J. Atmos. Sci.,* **43,** 802–822.

Braun, S. A., 2006: High-resolution simulation of Hurricane Bonnie (1998). Part II: Water budget. *J. Atmos. Sci.,* **63,** 43–64.

Doswell, C. A., III, H. E. Brooks, and R. A. Maddox, 1996: Flash flood forecasting: An ingredients-based methodology. *Wea. Forecasting,* **11,** 560–581.

Dudhia, J., 1993: A nonhydrostatic version of the Penn State/NCAR mesoscale model: Validation tests and simulation of an Atlantic cyclone and cold front. *Mon. Wea. Rev.,* **121,** 1493–1513.

Ferrier, B. S., J. Simpson, and W.-K. Tao, 1996: Factors responsible for precipitation efficiencies in midlatitude and tropical squall simulations. *Mon. Wea. Rev.,* **124,** 2100–2125.

Gamache, J. F., R. A. Houze Jr., and F. D. Marks Jr., 1993: Dual-aircraft investigation of the inner core of Hurricane Norbert. Part III: Water budget. *J. Atmos. Sci.,* **50,** 3221–3243.

Grell, G. A., J. Dudhia, and D. R. Stauffer, 1995: A description of the fifth-generation Penn State/NCAR Mesoscale Model. NCAR Tech. Note, 138 pp.

Hawkins, H. F., and S. M. Imbembo, 1976: The structure of a small, intense hurricane—Inez 1966. *Mon. Wea. Rev.,* **104,** 418–442.

Houze, R. A., Jr., F. D. Marks Jr., and R. A. Black, 1992: Dual-aircraft investigation of the inner core of Hurricane Norbert. Part II: Mesoscale distribution of ice particles. *J. Atmos. Sci.,* **49,** 943–962.

Kurihara, Y., 1975: Budget analyses of a tropical cyclone simulated in an axisymmetric numerical model. *J. Atmos. Sci.,* **32,** 25–59.

Li, M.-H., M.-J. Yang, R. Soong, and H.-L. Huang, 2005: Simulating typhoon floods with gauge data and mesoscale modeled rainfall in a mountainous watershed. *J. Hydrometeor.,* **6,** 306–323.

Li, X., C.-H. Sui, and K.-M. Lau, 2002: Precipitation efficiency in the tropical deep convective regime: A 2-D cloud resolving modeling study. *J. Meteor. Soc. Japan,* **80,** 205–212.

Liu, Y., D.-L. Zhang, and M. K. Yau, 1999: A multiscale numerical study of Hurricane Andrew (1992). Part II: Kinematics and inner-core structures. *Mon. Wea. Rev.,* **127,** 2597–2616.

Malkus, J., and H. Riehl, 1960: On the dynamics and energy transformations in steady-state hurricanes. *Tellus,* **12,** 1–20.

Marks, F. D., Jr., 1985: Evolution of the structure of precipitation in Hurricane Allen (1980). *Mon. Wea. Rev.,* **113,** 909–930.

——, and R. A. Houze Jr., 1987: Inner core structure of Hurricane Alicia from airborne Doppler radar observations. *J. Atmos. Sci.,* **44,** 1296–1317.

McFarquhar, G. M., and R. A. Black, 2004: Observations of particle size and phase in tropical cyclones: Implications for mesoscale modeling of microphysical processes. *J. Atmos. Sci.,* **61,** 422–439.

Reisner, J., R. J. Rasmussen, and R. T. Bruitjes, 1998: Explicit forecasting of supercooled liquid water in winter storms using the MM5 mesoscale model. *Quart. J. Roy. Meteor. Soc.,* **124,** 1071–1107.

Riehl, H., and J. S. Malkus, 1961: Some aspects of Hurricane Daisy, 1958. *Tellus,* **13,** 181–213.

Sui, C.-H., and Coauthors, 2002: Typhoon Nari and Taipei flood—A pilot meteorology-hydrology study. *Eos, Trans. Amer. Geophys. Union,* **83,** 265–270.

——, X. Li, M.-J. Yang, and H.-L. Huang, 2005: Estimation of oceanic precipitation efficiency in cloud models. *J. Atmos. Sci.,* **62,** 4358–4370.

——, ——, and ——, 2007: On the definition of precipitation efficiency. *J. Atmos. Sci.,* **64,** 4506–4513.

Tao, W.-K., and J. Simpson, 1993: Goddard Cumulus Ensemble model. Part I: Model description. *Terr. Atmos. Oceanic Sci.,* **4,** 35–72.

Yang, M.-J., D.-L. Zhang, and H.-L. Huang, 2008: A modeling study of Typhoon Nari (2001) at landfall. Part I: The topographic effects. *J. Atmos. Sci.,* **65,** 3095–3115.

——, ——, X.-D. Tang, and Y. Zhang, 2011: A modeling study of Typhoon Nari (2001) at landfall: 2. Structural changes and terrain-induced asymmetries. *J. Geophys. Res.,* **116,** D09112, doi:10.1029/2010JD015445.

Zhang, D.-L., Y. Liu, and M. K. Yau, 2000: A multiscale numerical study of Hurricane Andrew (1992). Part III: Dynamically induced vertical motion. *Mon. Wea. Rev.,* **128,** 3772–3788.

——, ——, and ——, 2001: A multiscale numerical study of Hurricane Andrew (1992). Part IV: Unbalanced flows. *Mon. Wea. Rev.,* **129,** 92–107.

——, ——, and ——, 2002: A multiscale numerical study of Hurricane Andrew (1992). Part V: Inner-core thermodynamics. *Mon. Wea. Rev.,* **130,** 2745–2763.